High-Q Mie resonators for refractive-index sensing

Esmaeel Zanganeh[1,*], Zarina Sadrieva[1], Polina Kapitanova[1], and Andrey Bogdanov[1,2]

[1]*School of Physics and Engineering, ITMO University, Saint Petersburg 197101, Russia*

[2]*Qingdao Innovation and Development Base of Harbin Engineering University, Qingdao, Shandong 266000, China*

Refractive-index sensors have been used in a wide range of applications, including biological diagnosis and therapy, material analysis and shaping, (bio)chemical sensing, environmental monitoring, and many more. A good sensor should have sufficiently high sensitivity and figures of merit to detect the slightest changes in the environment. Here, we study the performance of high-Q Mie modes of dielectric cylinders with ultrahigh permittivity for refractive-index sensing. First, we experimentally demonstrate the emergence of high-Q Mie modes in the scattering spectrum of a single dielectric cylinder with ultrahigh permittivity ($\varepsilon \approx 40$–100). We also investigate the sensitivity of the high-Q Mie modes to the background refractive index of the surrounding environment. The simulation results demonstrate that the high-Q Mie modes are sensitive to changes in the surrounding refractive index. This results in high sensitivities and remarkable figures of merit, indicating their potential for refractive-index sensing applications. However, the material losses limit the observation of high-Q modes and their sensing capability.

I. INTRODUCTION

Refractive-index (RI) sensors have found a wide range of applications in petroleum, chemical, biological, food, pharmaceutical, and environmental monitoring [1–9]. In particular, microwave sensors provide the benefits of good sensitivity, an excellent ability to perform in many environments, and easy fabrication and measurement [6]. Many RI sensors based on metamaterials with different configurations have been proposed [10–14]. However, these sensors are limited in sensitivity and figure of merit (FOM) due to their intrinsic losses and inherently low quality factors.

Dielectric resonators with a high Q factor are in high demand due to their ability to achieve exceptional energy confinement and minimal losses. This quality makes them valuable for various applications, including RI sensors [15]. The most widespread types of high-Q resonators are photonic crystal cavities [16] and the whispering-gallery [17] and Fabry-Perot [18] types. Their common disadvantage is that their Q factors drop drastically when the size of the cavity becomes subwavelength. This challenging task can be overcome with the concept of the *bound state in the continuum* (BIC) [19–22]. BICs become the focus of attention in the design of high-Q-factor resonators. Quasi-BIC in a single dielectric cylinder, which appeared from destructive interference between Mie and Fabry-Perot modes, provides a radiation Q factor as high a

s 63 700 [23]. The highest reached experimental value of the Q factor is about 12 500 and it has been limited by material losses in ceramic [24]. The designs of microcavities with quasi-BICs are very sensitive to the geometrical and material parameters and need very accurate fabrication. Recently, ceramic resonators with quasi-BICs have been used for highly sensitive chipless wireless temperature sensors [25].

Recent studies have demonstrated various RI sensors that exploit Mie modes [26–30]. The RI sensing is usually based on the detection of the spectral shift of the resonances induced by a change in the RI of the environment. Therefore, weak localization of the mode is desirable for a higher sensitivity. At the same time, weak localization of the mode inside the resonator decreases the Q factor, making the resonance broader and the FOM lower. A high FOM requires a high Q factor; however, if the radiative losses are much lower than the material losses, the high-Q mode is hardly observable in the experiment and it cannot be used for sensing. Thus, the optimal design of a highly sensitive sensor with a high FOM requires a fine balance between the radiative losses, material losses, and spatial confinement of the modes.

In this paper, we investigate the efficiency of high-Q Mie modes of different orders in low-loss and high-permittivity dielectric cylinders for RI sensing at microwave frequencies. We evaluate the sensitivity and the FOM of our dielectric cylinder sensors and compare them with state-of-the-art microwave RI sensors. We reveal the high

*esmaeelzanganeh@gmail.com

potential of our RI sensors based on high-Q dielectric resonators.

To understand the Mie modes, we begin with a theoretical investigation of the plane-wave scattering by a dielectric cylinder. Using the temporal coupled-mode theory, we can compute the scattering cross section (SCS) as follows [31]:

$$\sigma_{sc} = \frac{2\lambda}{\pi} \left| \frac{1}{2} \frac{(i(\omega_0 - \omega) + \gamma_{\text{abs}})(e^{i\phi} - 1) - \gamma_{\text{rad}}(1 + e^{i\phi})}{i(\omega_0 - \omega) + \gamma_{\text{abs}} + \gamma_{\text{rad}}} \right|^2,$$

(1)

where ϕ is a real phase factor, ω_0 is the resonant angular frequency, γ_{abs} is the intrinsic loss rate due to material absorption, and γ_{rad} is the external leakage rate due to the coupling of the resonance to the outgoing wave. Assuming that $\phi = 0$, the SCS spectrum has a Lorentzian shape [31]. We calculate the SCS at the resonance frequency by setting $\omega = \omega_0$ and simplifying Eq. (1) as follows:

$$\sigma_{sc} = \frac{2\lambda}{\pi} \left| \frac{-\gamma_{\text{rad}}}{\gamma_{\text{abs}} + \gamma_{\text{rad}}} \right|^2.$$

(2)

For the lower-order Mie modes excited in a dielectric particle with a relatively low permittivity ($\varepsilon \to 1$), the radiative loss is very high (i.e., when $\gamma_{\text{rad}} \gg \gamma_{\text{abs}}$) and one can rewrite Eq. (2) as

$$\sigma_{sc} \approx \frac{2\lambda}{\pi}.$$

(3)

For higher-order Mie modes excited in a dielectric particle with a huge permittivity ($\varepsilon \to \infty$), i.e., $\gamma_{\text{rad}} \ll \gamma_{\text{abs}}$, one obtains

$$\sigma_{sc} \to 0.$$

(4)

There is a critical coupling condition in which $\gamma_{\text{rad}} = \gamma_{\text{abs}}$. In this case,

$$\sigma_{sc} \approx \frac{\lambda}{2\pi}.$$

(5)

II. NUMERICAL STUDY OF SCATTERING AND ABSORPTION CROSS SECTIONS

We start our study with numerical simulations of the SCS and absorption cross section (ACS) of a finite dielectric cylinder with permittivity ε varying from 30 to 500, loss tangent $\tan\delta = 2.5 \times 10^{-4}$, radius R, and height h, placed in a medium with permittivity $\varepsilon_s = 1$, as shown in Fig. 1. To keep the same frequency range for different ε,
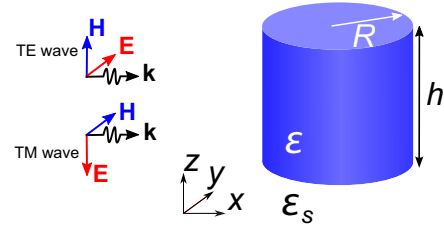

FIG. 1.   A schematic view of a dielectric cylinder resonator with permittivity ε, radius R, and height h, placed in a medium with permittivity $\varepsilon_s = 1$ under TE- and TM-polarized incident plane waves.

the following relations between ε, R, and h are set:

$$R = \frac{110}{\varepsilon}(\text{mm}) \quad \text{and} \quad h = \frac{R}{4}(\text{mm}) \quad \text{for a TE wave,}$$

$$R = \frac{145}{\varepsilon}(\text{mm}) \quad \text{and} \quad h = \frac{R}{2}(\text{mm}) \quad \text{for a TM wave.}$$

(6)

The SCS and ACS of the cylinders with permittivity ε varying from 30 to 500 under the excitation of TE- and TM-polarized plane waves are calculated by the frequency-domain solver of CST MICROWAVE STUDIO 2022. To compare the ACS and SCS for cylinders with different aspect ratios, we normalize the ACS and SCS by the projected cross section of the resonator, $P = 2Rh$. The results are shown in Figs. 2(a) and 2(b). For TE-polarized excitation, the first resonance occurs at around 2.2 GHz [Fig. 2(a)]. The calculated electric field distribution of this resonance at the x-y plane demonstrated in Fig. 2(a) shows that the magnetic dipole (MD) mode is excited. As ε increases from 30 to 500, the resonance becomes narrower in bandwidth (higher in Q factor). For $\varepsilon < 500$, the absorption loss (ACS) is lower than the radiation loss (SCS), the condition $\gamma_{\text{rad}} \gg \gamma_{\text{abs}}$ is satisfied, and the mode has a low Q factor with a high SCS [Eq. (3)]. For the resonance at around 3.4 GHz [indicated by pink arrows in Fig. 2(a)], the electric field distribution demonstrated in Fig. 2(a) indicates that the electric quadrupole (EQ) mode is excited inside the cylinder. For $\varepsilon = 30$, $\gamma_{\text{rad}} \gg \gamma_{\text{abs}}$, and by increasing ε, the absorption loss increases, satisfying the critical coupling condition $\gamma_{\text{rad}} = \gamma_{\text{abs}}$ at $\varepsilon = 100$. Further increase of ε leads to the disappearance of the enhancement in the SCS for $\varepsilon = 200$ and $\varepsilon = 500$, where $\gamma_{\text{abs}} > \gamma_{\text{rad}}$. Narrow ACS resonances indicate that the mode remains excited inside the cylinder. However, its radiation is too low to be detected due to the extremely high ε and, thus, the mode is quasi-non-radiative.

The next resonance at around 3.95 GHz [indicated by green arrows in Fig. 2(a)] is electric octupole (EO). For $\varepsilon = 30$, $\gamma_{\text{rad}} = \gamma_{\text{abs}}$, satisfying the critical coupling condition. For $\varepsilon \geq 50$, the mode is quasi-non-radiative. The
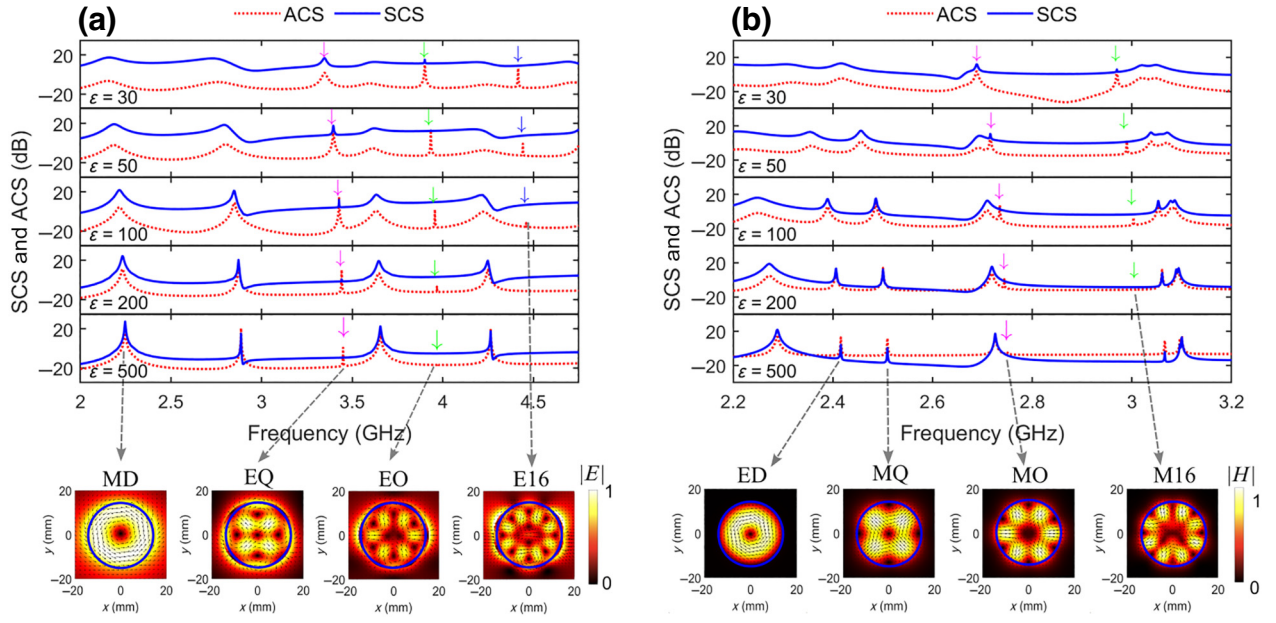
FIG. 2. (a) The simulated SCS (blue line) and ACS (dotted orange line) of the dielectric cylinders with permittivity $\varepsilon = 30, 50$, 100, 200, and 500 and loss tangent $\tan \delta = 2.5 \times 10^{-4}$, normalized to the projected cross section $P = 2Rh$ under TE-polarized plane-wave illumination. The insets show simulated electric field distributions of the MD, EQ, EO, and E16 modes. (b) The simulated SCS (blue line) and ACS (dotted orange line) of the dielectric cylinders with permittivity $\varepsilon = 30, 50, 100, 200$, and 500 and loss tangent $\tan \delta = 2.5 \times 10^{-4}$, normalized to the projected cross section $P = 2Rh$ under TM-polarized plane-wave illumination. The insets show simulated magnetic field distributions of the ED, MQ, MO, and M16 modes.

last mode excited around 4.45 GHz is electric 16-pole (E16) [see Fig. 2(a)] and is already quasi-non-radiative for $30 \leq \varepsilon \leq 100$. We should note that for $\varepsilon = 200$ and $\varepsilon = 500$, the ACS enhancement also vanishes, indicating that the mode is not excited.

For TM-polarized excitation, based on the calculated magnetic field distributions at the x-y plane demonstrated in Fig. 2(b), the electric dipole (ED) mode is excited at around 2.4 GHz. As ε increases from 30 to 200, the resonance becomes narrower in bandwidth (higher in Q factor), since the ACS (γ_{abs}) increases, leading to satisfying the critical coupling condition $\gamma_{\text{rad}} = \gamma_{\text{abs}}$ at $\varepsilon \approx 200$. However, it never becomes quasi-non-radiative. The magnetic quadrupole (MQ) mode excited between 2.45 and 2.5 GHz shows the same behavior as the ED mode. However, the magnetic octupole (MO) mode [indicated by pink arrows in Fig. 2(b)] is becoming quasi-non-radiative for $\varepsilon \geq 100$. The mode excited at around 3 GHz [green arrows in Fig. 2(b)] is magnetic 16-pole (M16) [see the corresponding fields in Fig. 2(b)] and is quasi-non-radiative for $50 \leq \varepsilon < 500$. Note that for $\varepsilon = 500$, the enhancement in the ACS also disappears, showing that this mode is not excited.

III. EXPERIMENTAL STUDY OF SCATTERING CROSS SECTION AND NEAR-FIELD DISTRIBUTION

We perform the experimental study to demonstrate the existence of high-Q and quasi-non-radiative modes of the

dielectric cylinders with high permittivities under TE-polarized plane-wave excitation. Three ceramic cylinders with permittivities $\varepsilon = 40, 80$, and 100 and geometrical parameters listed in Table I of the Supplemental Material [32], have been fabricated. To measure the SCS, the prototype is placed in the middle of two horn antennas, and the forward scattering is measured [33,34]. A photograph of the experimental setup for measuring the SCS of the cylinder prototypes is shown in the top subplot of Fig. 3(a) (for details, see Sec. I of the Supplemental Material [32]). The measured SCSs of cylinders with permittivities $\varepsilon = 40, 80$, and 100 are compared with the numerical results in the middle subpanels of Figs. 3(b)–3(d), respectively. Good agreement is achieved. The calculated ACSs of the cylinders with permittivities $\varepsilon = 40, 80$, and 100 are shown in the top subpanels of Figs. 3(b)–3(d), respectively. We have also measured the normal component of the magnetic field at the x-y plane 4 mm above the surface of the cylinders using a near-field mapping procedure. A photograph of the experimental setup is shown in the bottom subplot of Fig. 3(a) (for details, see Sec. I of the Supplemental Material [32]). The results are compared with the simulated ones in Figs. 3(b)–3(d). For the cylinder with $\varepsilon = 40$, as predicted numerically, all the MD, EQ, EO, and E16 modes are observed in the magnetic field distributions. The E16 mode is quasi-non-radiative, since the SCS shows no enhancement at the frequency of interest [5.9 GHz in Fig. 3(b)]. For the cylinder with $\varepsilon = 80$, both E16 and EO become quasi-non-radiative [see the SCS in
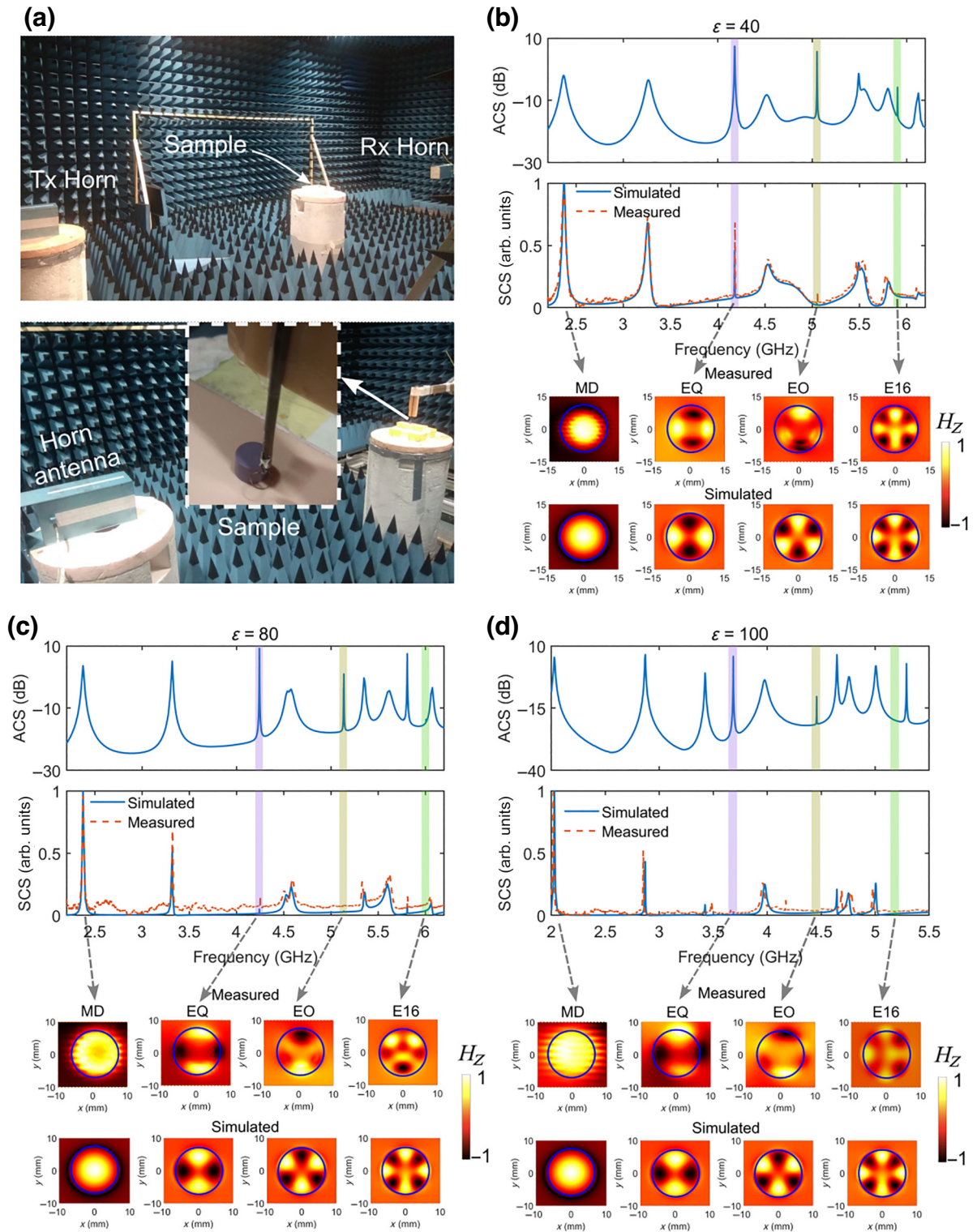
FIG. 3.   (a) Photographs of the experimental setups to measure the SCS and the near magnetic field distribution of the cylinder prototypes. Here, the prototypes are excited from the side with a TE-polarized wave. The inset represents the cylinder prototype with a permittivity of $\varepsilon = 100$, a radius of $R = 7$ mm, and a height of $h = 10$ mm. Top subplots: the simulated ACS of the dielectric cylinders with (b) permittivity $\varepsilon = 40$ and loss tangent $\tan \delta = 2.5 \times 10^{-4}$, (c) permittivity $\varepsilon = 80$ and loss tangent $\tan \delta = 4 \times 10^{-4}$, and (d) permittivity $\varepsilon = 100$ and loss tangent $\tan \delta = 7 \times 10^{-4}$, normalized to the projected cross section $P = 2Rh$ under TE-polarized plane-wave excitation. Middle subplots: the measured (dotted orange lines) and simulated (blue lines) SCS of the cylinders with the (b) permittivity $\varepsilon = 40$ and loss tangent $\tan \delta = 2.5 \times 10^{-4}$, (c) permittivity $\varepsilon = 80$ and loss tangent $\tan \delta = 4 \times 10^{-4}$, and (d) permittivity $\varepsilon = 100$ and loss tangent $\tan \delta = 7 \times 10^{-4}$. Bottom subplots: the measured and simulated normal component of the magnetic fields for the MD, EQ, EO, and E16 modes at 4 mm above the cylinder surface, with (b) $\varepsilon = 40$, (c) $\varepsilon = 80$, and (d) $\varepsilon = 100$.
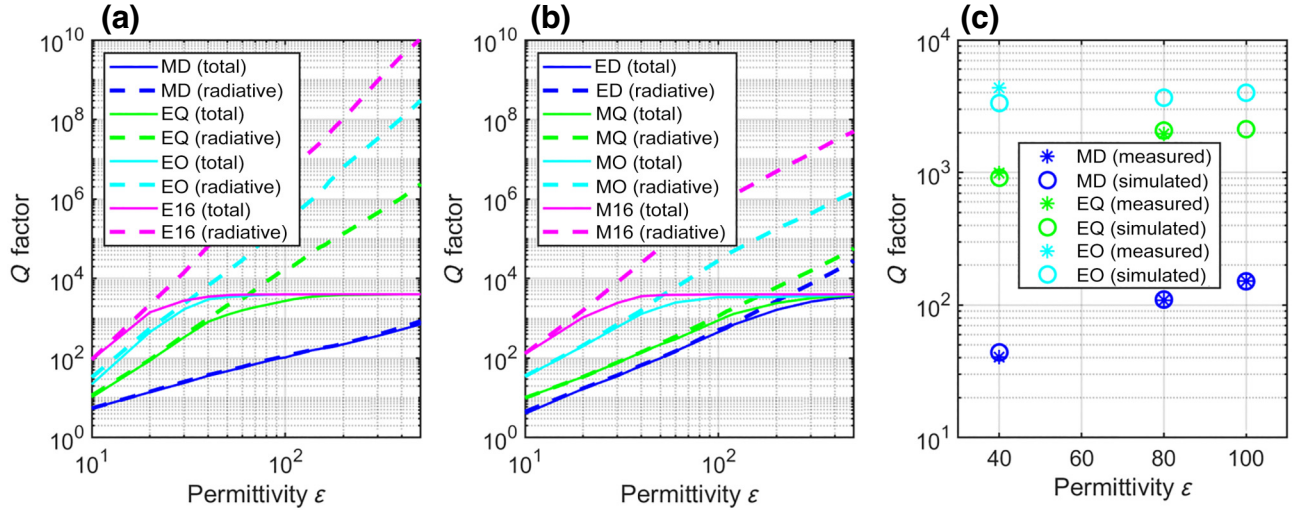
FIG. 4. The simulated radiative (dashed lines) and total (solid lines) Q factors of (a) the MD, EQ, EO, and E16 and (b) the ED, MQ, MO, and M16 modes as functions of the cylinder permittivity for loss tangent $\tan\delta = 2.5 \times 10^{-4}$. (c) The measured and simulated total Q factors of the MD, EQ, and EO modes of the dielectric cylinders with a permittivity of $\varepsilon = 40$ ($\tan\delta = 2.5 \times 10^{-4}$), $\varepsilon = 80$ ($\tan\delta = 4 \times 10^{-4}$), and $\varepsilon = 100$ ($\tan\delta = 7 \times 10^{-4}$), respectively.

Fig. 3(c)], whereas for the cylinder with $\varepsilon = 100$, the EQ, EO, and E16 modes are quasi-non-radiative [the SCS in Fig. 3(d)].

IV. Q-FACTOR ANALYSIS

Here, we analyze the effect of the cylinder permittivity on the Q factor of the Mie modes. Figure 4(a) shows the simulated total and radiative Q factors of the MD, EQ, EO, and E16 modes as a function of the cylinder permittivity ε. The material loss tangent for all permittivities is set as $\tan\delta = 2.5 \times 10^{-4}$. The total and radiative Q factors of the MD mode increase by increasing the permittivity and reach 650 and 774 at $\varepsilon = 500$, respectively. For the EQ mode, the radiative Q factor reaches 2.17×10^{6} at $\varepsilon = 500$. However, the total Q factor is saturated to $1/\tan\delta = 4000$ due to the material loss. One can see that the radiative Q factors of the EO and E16 modes increase by increasing ε and reach 2.99×10^{8} and 1×10^{10}, respectively. Nevertheless, their total Q factors are saturated to $1/\tan\delta = 4000$. Figure 4(b) shows the simulated total and radiative Q factors of the ED, MQ, MO, and M16 modes on the permittivity of the cylinder ε. The radiative Q factors of the ED, MQ, MO, and M16 modes reach 2.8×10^{4}, 5.7×10^{4}, 1.5×10^{6}, and 5×10^{7}, respectively. Their total Q factors are all saturated to 4000. To achieve a higher total Q factor of all modes, one should use material with lower loss in addition to using a higher permittivity ε.

To validate the Q factors of the MD, EQ, and EO modes of the cylinders with permittivities 40, 80, and 100 predicted numerically, we compare them with the Q factors obtained from the measured SCS. The Q-factor

extraction method is described in Sec. I of the Supplemental Material [32]. Figure 4(c) demonstrates good agreement between the values obtained numerically and experimentally.

V. SENSING APPLICATION

Finally, we investigate the sensing performance of the high-Q Mie resonances in the RI sensing application. Extinction cross sections (ECSs) normalized to the projected cross section $P = 2Rh$ under TM-polarized excitation around the MQ mode of the cylinder with permittivities $\varepsilon = 40, 80, 120, 160, 200, 240,$ and 280, placed in a medium with a permittivity ε_s changing from 1 to 1.04 are calculated in CST MICROWAVE STUDIO. A schematic view of the structure is shown in the inset of Fig. 5(b). The results for lossy ($\tan\delta = 2.5 \times 10^{-4}$) and lossless cylinder materials are shown in Figs. 5(a) and 5(b), respectively. For the lossy case [Fig. 5(a)], one can easily see that the MQ resonant frequency shifts by changing the surrounding medium permittivity ε_s for all values of the cylinder permittivity ε, showing the good sensitivity of the MQ mode. However, by increasing ε, the maximum ECS first increases (for $\varepsilon \leq 160$) and then decreases (for $\varepsilon \geq 160$). For the lossless case [Fig. 5(b)], beyond the same sensitivity as the lossy one, narrower resonances are observed for high ε, which helps to distinguish the deviations better. The same ECS plots for different ε and ε_s around other modes (ED, MD, EQ, MO, and EO) are shown in Sec. II of the Supplemental Material [32].

RI sensors are often quantitatively compared by their RI sensitivity. Here, we define the RI sensitivity as the shift
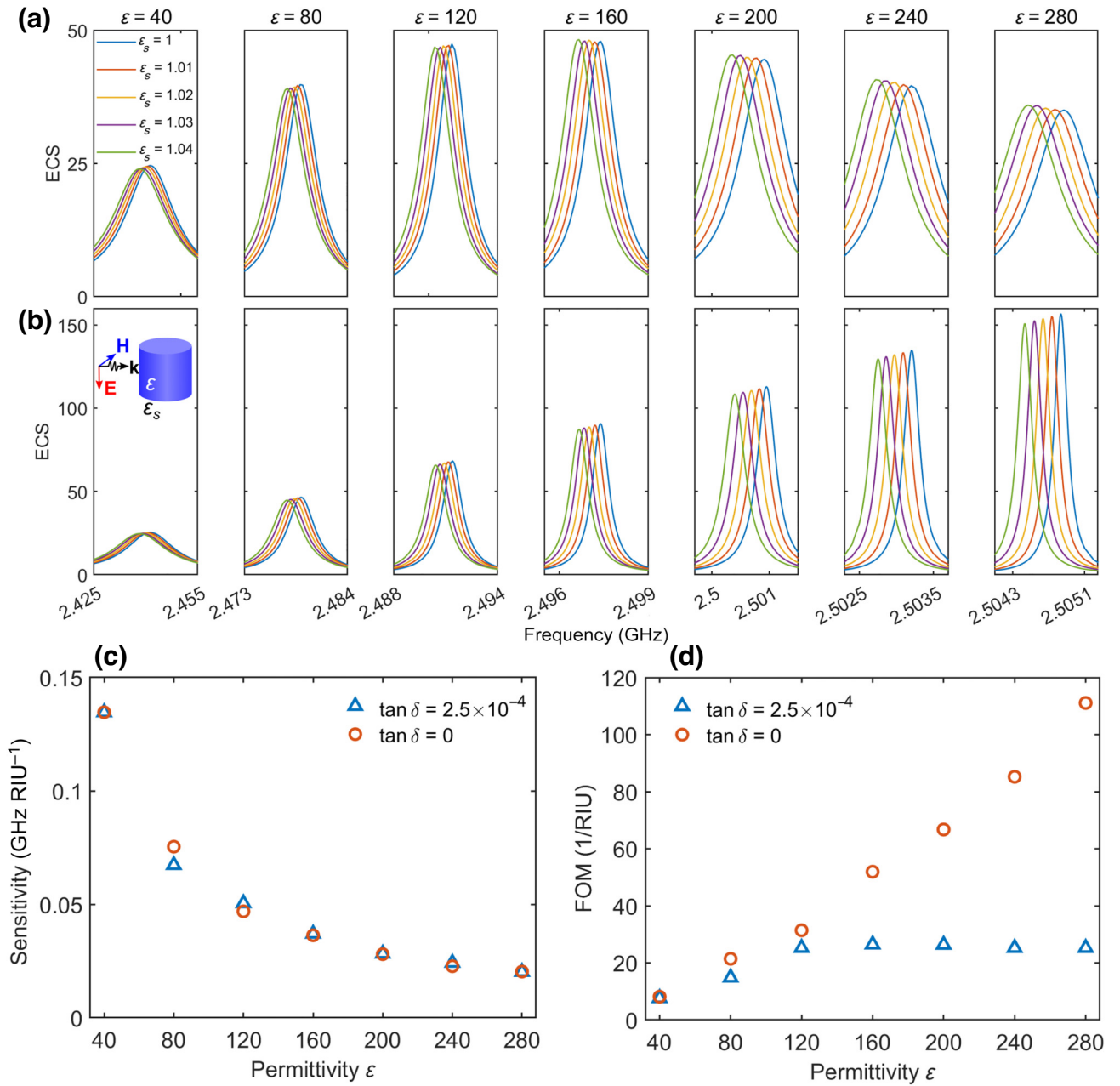
FIG. 5. (a) The simulated ECSs normalized to the projected cross section $P = 2Rh$ for the cylinders with permittivities of $\varepsilon = 40$, 80, 120, 160, 200, 240, and 280 and loss tangent $\tan\delta = 2.5 \times 10^{-4}$, placed in a medium with background permittivities of $\varepsilon_s = 1$, 1.01, 1.02, 1.03, and 1.04 around the MQ resonance. (b) The simulated ECSs normalized to the projected cross section $P = 2Rh$ for the cylinders with the same parameters as in (a) but with the zero loss tangent. (c) The sensitivity of the MQ mode of the cylinders in (a) and (b) as a function of the cylinder permittivity calculated using Eq. (7). (d) The FOM of the MQ mode of the cylinders in (a) and (b) as a function of the cylinder permittivity calculated using Eq. (8).

of the resonant frequency versus the change in RI of the surrounding medium as follows [35]:

$$S = \frac{\Delta f}{\Delta n_s} \quad \left(\frac{\text{GHz}}{\text{RIU}}\right), \tag{7}$$

where Δf denotes the deviation of the resonant frequency, Δn_s is the deviation of the RI of the surrounding medium,

and RIU is refractive index unit. The RI sensitivities of the MQ mode as a function of ε for the lossless and lossy materials with loss tangent $\tan\delta = 2.5 \times 10^{-4}$ are shown in Fig. 5(c). By increasing ε, the sensitivity decreases.

The ability of a sensor to detect slight changes in the RI is proportional directly to S and inversely to the width of the resonant peak or dip being tracked. The combination of these parameters is known as the FOM and is represented

TABLE I. The sensitivity (S), FHBW, FOM, and ECS$_{max}$ of the ED, MD, EQ, MQ, EO, and MO modes for cylinder permittivities of $\varepsilon = 40, 80, 120, 160, 200, 240,$ and 280. The loss tangent is $\tan \delta = 2.5 \times 10^{-4}$.

Mode	S, FHBW, FOM, and ECS	$\varepsilon = 40$	$\varepsilon = 80$	$\varepsilon = 120$	$\varepsilon = 160$	$\varepsilon = 200$	$\varepsilon = 240$	$\varepsilon = 280$
ED	S (GHz RIU^{-1})	0.16	0.09	0.06	0.04	0.03	0.03	0.02
	FHBW (MHz)	40	8.8	3.7	2	1.5	1.2	1
	FOM (RIU^{-1})	4	10.7	16	22.2	21.6	22.6	24.2
	ECS$_{max}$	18	27.9	36	40.3	41.2	39.7	37.3
MD	S (GHz RIU^{-1})	0.1	0.1	0.1	0.05	0.05	0.03	0.03
	FHBW (MHz)	102	46	26	19	15	11	10
	FOM (RIU^{-1})	1	2.2	3.9	2.6	3.4	3.1	2.7
	ECS$_{max}$	63.3	116.9	170.7	223.2	273.7	325.1	377.7
EQ	S (GHz RIU^{-1})	0.2	0.08	0.05	0.03	0.03	0.03	0.02
	FHBW (MHz)	9	2	1	0.9	0.8	0.8	0.8
	FOM (RIU^{-1})	19.6	47.5	47.3	40.2	36.07	30.1	18.5
	ECS$_{max}$	56.6	111.9	34.7	19.7	11.9	7.7	5.5
MQ	S (GHz RIU^{-1})	0.1	0.07	0.05	0.04	0.03	0.02	0.02
	FHBW (MHz)	17.6	4.5	2	1.4	1.1	1	0.8
	FOM (RIU^{-1})	7.6	14.8	25.2	26.4	26.3	25.2	25.2
	ECS$_{max}$	24.6	39.8	47.4	48.3	44.5	39.6	35
EO	S (GHz RIU^{-1})	0.1	0.05	0.04	0.03	0.02	0.02	0.02
	FHBW (MHz)	1.8	1	1	1	0.9	0.9	0.9
	FOM (RIU^{-1})	70	54.5	37.9	26.7	22.8	20	16.3
	ECS$_{max}$	36.5	16.2	7	4.1	2.2	1.5	1
MO	S (GHz RIU^{-1})	0.1	0.05	0.03	0.02	0.02	0.01	0.01
	FHBW (MHz)	2.2	0.9	0.8	0.7	0.6	0.6	0.2
	FOM (RIU^{-1})	45.9	54.4	40.4	35.9	30.3	22.8	55.3
	ECS$_{max}$	20.7	11.7	5.6	3.2	2.8	1.4	1.1

as [35]:

$$\mathrm{FOM} = \frac{S}{\mathrm{FHBW}} \quad \left(\frac{1}{\mathrm{RIU}} \right), \qquad (8)$$

where FHBW is the full width at half maximum of the ECS spectrum. The FOMs of the MQ mode as a function of ε for the lossless and lossy materials with loss tangent $\tan \delta = 2.5 \times 10^{-4}$ are shown in Fig. 5(d). One can see that although the sensitivities of both the lossless and the lossy cases decrease by increasing ε, the FOM increases linearly in the lossless case and saturates to 25 (RIU^{-1}) in the lossy case for $\varepsilon \geq 120$. Therefore, $\varepsilon = 120$ is the optimum choice in terms of the sensitivity and the FOM of the MQ mode. The frequency sensitivity and FOM of other modes are discussed in Sec. II of the Supplemental Material [32].

Table I lists the RI sensitivity, FHBW, FOM, and ECS$_{max}$ of the Mie modes for $\varepsilon = 40, 80, 120, 160,$ 240, and 280 and loss tangent $\tan \delta = 2.5 \times 10^{-4}$. For the ED mode, as ε increases, the sensitivity and ECS$_{max}$ gradually decrease. The FOM increases up to 24.2 (RIU^{-1}) for $\varepsilon = 280$. Having relatively good sensitivity, a high FOM, and sufficient ECS$_{max}$ (for easily detectable resonance), the optimum value of the cylinder permittivity for the ED mode is $\varepsilon = 160$. Other modes provide the same behavior as the ED regarding the sensitivity, FOM, and

ECS$_{max}$. The best sensitivity performance of each mode is achieved at the optimum permittivity. The corresponding sensitivity, FHBW, FOM, and ECS$_{max}$ values are written in blue. The maximum FOM achieved is 70 (RIU^{-1}), which corresponds to the EO mode of the cylinder with $\varepsilon = 40$.

Next, we numerically study how the aspect ratio of the cylinder affects the sensing performance of the MQ mode. We place a cylinder with permittivity $\varepsilon = 120$ and loss tangent $\tan \delta = 2.5 \times 10^{-4}$ in two different background media, with permittivities of $\varepsilon_s = 1$ and 1.04, vary the aspect ratio R/h of the cylinder from 1 to 4.5, and calculate the ECS around the MQ mode under TM-polarized excitation. The calculated ECS results are given in Fig. S7(a) of the Supplemental Material [32]. Figure 6(a) shows how the sensitivity and the FOM change with the aspect ratio R/h. The sensitivity increases as the aspect ratio increases because a larger aspect ratio means a larger surface area of the cylinder that interacts with the surrounding medium (localized fields are accumulated near the cylinder surfaces). However, the FOM has maximum values at $R/h = 1.5$ and 2 and then decreases for larger aspect ratios. This means that there is an optimal aspect ratio that maximizes the sensing performance of the cylinder.

We also investigate how the sensitivity of the dielectric cylinder to a thin analyte layer depends on the permittivity of the cylinder and the layer thickness using
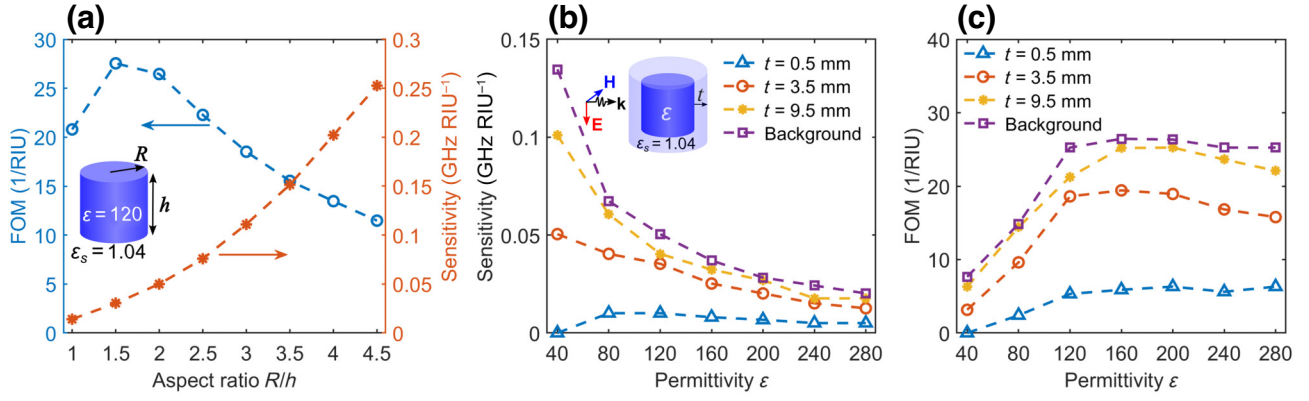
FIG. 6. (a) The sensitivity and FOM of the MQ mode of the cylinder with permittivity $\varepsilon = 120$ and loss tangent $\tan \delta = 2.5 \times 10^{-4}$ as a function of the cylinder aspect ratio R/h. (b),(c) The sensitivity (b) and the FOM (c) of the MQ mode of the cylinders with permittivities of $\varepsilon = 40, 80, 120, 160, 200, 240,$ and 280 and loss tangent $\tan \delta = 2.5 \times 10^{-4}$ surrounded by a shell layer with thickness t and a permittivity of $\varepsilon_s = 1.04$.

numerical simulations. We take the MQ mode and use a TM-polarized plane wave to excite it. We consider cylinders with different permittivities ($\varepsilon = 40, 80, 120, 160, 200, 240,$ and 280) and a fixed loss tangent ($\tan \delta = 2.5 \times 10^{-4}$). We surround the cylinders with an analyte layer with a permittivity of $\varepsilon_s = 1.04$ and a variable thickness of t [see the inset of Fig. 6(b)]. We vary t from 0 to 9.5 mm and calculate the ECS. The results are shown in Fig. S7(b) of the Supplemental Material [32]. Figures 6(b) and 6(c) show the sensitivity and the FOM as a function of the cylinder permittivity for different values of t. For all values of t, the sensitivity decreases as the permittivity of the cylinder increases and the FOM saturates for $\varepsilon \geq 120$, the same as the case when the entire surrounding medium has a permittivity of 1.04. The sensitivity and the FOM increase as t increases and they approach the values of the case in which the entire surrounding medium has a permittivity of 1.04 [the purple curve in Figs. 6(b) and 6(c)] for $t = 9.5$ mm for all cylinder permittivities.

Furthermore, we compare the sensitivity and the FOM of different RI sensors in the gigahertz and terahertz frequency ranges, which have been previously reported, with our proposed cylinder operating in the EO mode with $\varepsilon = 40$ in Table II. For a fair comparison, we normalize the size of the sensors to the resonance wavelength. First, we note that the normalized size of our sensor is one order of magnitude smaller than the unit-cell sizes of all other reported sensors, which enables sensing at a very small scale. Second, although the sensitivity of our structure is lower than the sensor reported in Ref. [10], it is comparable to other reported sensors in the gigahertz range [11,12]. The main advantage of our proposed sensor is its very high FOM compared to all previously reported sensors in both the gigahertz and terahertz ranges [10–12,35–40].

In practical applications, our proposed RI sensors will be placed in a background medium with an unknown RI, which affects the resonance frequency of the Mie modes. By measuring the SCS spectrum of the device, one can extract the resonance frequency and then calculate the RI

TABLE II. A comparison of the sensing performance of the high-Q Mie modes with other RI sensors.

Reference	Frequency	Size/λ	S	FOM (RIU^{-1})
[10]	5.2 (GHz)	0.43 (unit cell)	32.6 (GHz RIU^{-1})	11.9
[11]	9 (GHz)	0.36 (unit cell)	1.3 (GHz RIU^{-1})	7.3
[12]	9.3 (GHz)	0.56 (unit cell)	2.4 (GHz RIU^{-1})	4.9
[36]	0.5 (THz)	0.58 (unit cell)	0.023 (THz RIU^{-1})	$\cdots$
[35]	5.66 (THz)	0.28 (unit cell)	0.87 (THz RIU^{-1})	26.51
[37]	0.68 (THz)	0.41 (unit cell)	0.096 (THz RIU^{-1})	7.8
[38]	1.85 (THz)	0.37 (unit cell)	0.152 (THz RIU^{-1})	4.26
[39]	2.249 (THz)	0.27 (unit cell)	0.3 (THz RIU^{-1})	2.94
[40]	0.81 (THz)	0.49 (unit cell)	0.105 (THz RIU^{-1})	7.5
This work (EO)	3.9 (GHz)	0.07	0.1 (GHz RIU^{-1})	70

of the background medium using a calibration curve or a fitting function [41–43].

VI. CONCLUSIONS

We have developed a simple approach to exploring high-Q Mie modes in a single dielectric cylinder. The radiation Q factors of the E16 and M16 modes can be up to 1×10^{10} and 5×10^7, respectively. We have experimentally demonstrated the emergence of high-Q Mie modes in the scattering spectrum of single dielectric cylinders with ultrahigh permittivity. We have also studied the performance of the high-Q Mie modes in RI sensing. The simulated results demonstrate that the high-Q Mie modes are sensitive to slight changes in the surrounding RI, resulting in relatively good sensitivities (0.1 GHz RIU^{-1} for the EO mode) and large FOMs (70 RIU^{-1} for the EO mode), ensuring the potential application of the method in RI sensing.

[1] N. Kazanskiy, S. Khonina, and M. Butt, Plasmonic sensors based on metal-insulator-metal waveguides for refractive index sensing applications: A brief review, Phys. E: Low-Dimens. Syst. Nanostructures **117**, 113798 (2020).

[2] A. Dahlin, *Plasmonic Biosensors: An Integrated View of Refractometric Detection*, Advances in Biomedical Spectroscopy (Ios Press, 2012).

[3] S. A. Mitu, K. Ahmed, F. A. Al Zahrani, A. Grover, M. S. M. Rajan, and M. A. Moni, Development and analysis of surface plasmon resonance based refractive index sensor for pregnancy testing, Opt. Lasers. Eng. **140**, 106551 (2021).

[4] T. Parvin, K. Ahmed, A. M. Alatwi, and A. N. Z. Rashed, Differential optical absorption spectroscopy-based refractive index sensor for cancer cell detection, Opt. Rev. **28**, 134 (2021).

[5] X. Fan, I. M. White, S. I. Shopova, H. Zhu, J. D. Suter, and Y. Sun, Sensitive optical biosensors for unlabeled targets: A review, Anal. Chim. Acta. **620**, 8 (2008).

[6] R. A. Alahnomi, Z. Zakaria, Z. M. Yussof, A. A. Althuwayb, A. Alhegazi, H. Alsariera, and N. A. Rahman, Review of recent microwave planar resonator-based sensors: Techniques of complex permittivity extraction, applications, open challenges and future research directions, Sensors **21**, 2267 (2021).

[7] B.-F. Wan, Z.-W. Zhou, Y. Xu, and H.-F. Zhang, A theoretical proposal for a refractive index and angle sensor based on one-dimensional photonic crystals, IEEE Sens. J. **21**, 331 (2020).

[8] B.-F. Wan, Q.-Y. Wang, H.-M. Peng, H.-N. Ye, and H.-F. Zhang, A late-model optical biochemical sensor based on OTS for methane gas and glucose solution concentration detection, IEEE Sens. J. **21**, 21465 (2021).

[9] B.-F. Wan, H.-N. Ye, D. Zhang, and H. Zhang, A variable refractive index sensor based on epsilon-near-zero spatial selection structure and its potential in biological detection, New J. Phys. **25**, 023003 (2023).

[10] X. Q. Lin, Z. Chen, J. W. Yu, P. Q. Liu, P. F. Li, and Z. D. Chen, An EIT-based compact microwave sensor with double sensing functions, IEEE Sens. J. **16**, 293 (2015).

[11] W. Zhang, J.-y. Li, J. Xie, and R. Xu, High sensitivity refractive index sensor based on frequency selective surfaces absorber, IEEE Sens. Lett. **2**, 1 (2018).

[12] S. Hu and D. Liu, Dual-band microwave resonators based on cross hollow structures for refractive index sensing, Phys. Scr. **95**, 085504 (2020).

[13] S. K. Patel, N. Solanki, S. Charola, J. Parmar, R. Zakaria, O. S. Faragallah, M. M. Eid, and A. N. Z. Rashed, Graphene based highly sensitive refractive index sensor using double split ring resonator metasurface, Opt. Quantum Electron. **54**, 203 (2022).

[14] D. Hu, T. Meng, H. Wang, Y. Ma, and Q. Zhu, Ultra-narrow-band terahertz perfect metamaterial absorber for refractive index sensing application, Results Phys. **19**, 103567 (2020).

[15] F. Vollmer and L. Yang, Review label-free detection with high-Q microcavities: A review of biosensing mechanisms for integrated devices, Nanophotonics **1**, 267 (2012).

[16] Y. Akahane, T. Asano, B.-S. Song, and S. Noda, High-Q photonic nanocavity in a two-dimensional photonic crystal, Nature **425**, 944 (2003).

[17] K. J. Vahala, Optical microcavities, Nature **424**, 839 (2003).

[18] D. R. Abujetas, M. A. Mandujano, E. R. Méndez, and J. A. Sánchez-Gil, High-contrast Fano resonances in single semiconductor nanorods, ACS Photonics **4**, 1814 (2017).

[19] C. W. Hsu, B. Zhen, A. D. Stone, J. D. Joannopoulos, and M. Soljačić, Bound states in the continuum, Nat. Rev. Mater. **1**, 1 (2016).

[20] A. Kodigala, T. Lepetit, Q. Gu, B. Bahari, Y. Fainman, and B. Kanté, Lasing action from photonic bound states in continuum, Nature **541**, 196 (2017).

[21] Z. Liu, Y. Xu, Y. Lin, J. Xiang, T. Feng, Q. Cao, J. Li, S. Lan, and J. Liu, High-Q quasibound states in the continuum for nonlinear metasurfaces, Phys. Rev. Lett. **123**, 253901 (2019).

[22] K. Koshelev, A. Bogdanov, and Y. Kivshar, Meta-optics and bound states in the continuum, Sci. Bull. **64**, 836 (2019).

[23] M. V. Rybin, K. L. Koshelev, Z. F. Sadrieva, K. B. Samusev, A. A. Bogdanov, M. F. Limonov, and Y. S. Kivshar, High-Q supercavity modes in subwavelength dielectric resonators, Phys. Rev. Lett. **119**, 243901 (2017).

[24] M. Odit, K. Koshelev, S. Gladyshev, K. Ladutenko, Y. Kivshar, and A. Bogdanov, Observation of supercavity modes in subwavelength dielectric resonators, Adv. Mater. **33,** 2003804 (2021).

[25] I. Yusupov, D. Filonov, A. Bogdanov, P. Ginzburg, M. V. Rybin, and A. Slobozhanyuk, Chipless wireless temperature sensor based on quasi-BIC resonance, Appl. Phys. Lett. **119,** 193504 (2021).

[26] W. He, W. Zhang, J. Zhang, P. Yu, P. Liu, G. Yang, and H. Lei, Mie resonant scattering-based refractive index sensor using a quantum dots-doped polylactic acid nanowire, Appl. Phys. Lett. **119,** 111106 (2021).

[27] L. Ding, D. Eschimese, T. Y. L. Ang, D. Morits, H. S. Chu, S. T. Lim, C. E. Png, S. Gorelik, R. Paniagua-Dominguez, and A. I. Kuznetsov, One-dimensional high-Q silicon nanoparticle chain resonators for refractive index sensing, ACS Appl. Nano Mater. **5,** 3170 (2022).

[28] D. R. Abujetas, J. J. Sáenz, and J. A. Sánchez-Gil, Narrow Fano resonances in Si nanocylinder metasurfaces: Refractive index sensing, J. Appl. Phys. **125,** 183103 (2019).

[29] M. A. Abbas, A. Zubair, K. Riaz, W. Huang, J. Teng, M. Q. Mehmood, and M. Zubair, Engineering multimodal dielectric resonance of TiO_2 based nanostructures for high-performance refractive index sensing applications, Opt. Express **28,** 23509 (2020).

[30] W. Su, X. Chen, Z. Geng, Y. Luo, and B. Chen, Multiple Fano resonances in all-dielectric elliptical disk-ring metasurface for high-quality refractive index sensing, Results Phys. **18,** 103340 (2020).

[31] E. Kamenetskii, A. Sadreev, and A. Miroshnichenko, in *Fano Resonances in Optics and Microwaves: Physics and Applications* (Springer, Cham, Switzerland, 2018).

[32] See the Supplemental Material at http://link.aps.org/supplemental/10.1103/PhysRevApplied.21.024028 for details of the experimental study and sensitivity analysis results, which includes Refs. [46–52].

[33] A. A. Basharin, E. Zanganeh, A. K. Ospanova, P. Kapitanova, and A. B. Evlyukhin, Selective superinvisibility effect via compound anapole, Phys. Rev. B **107,** 155104 (2023).

[34] P. Kapitanova, E. Zanganeh, N. Pavlov, M. Song, P. Belov, A. Evlyukhin, and A. Miroshnichenko, Seeing the unseen: Experimental observation of magnetic anapole state inside a high-index dielectric particle, Ann. Phys. **532,** 2000293 (2020).

[35] Q. Shangguan, Z. Chen, H. Yang, S. Cheng, W. Yang, Z. Yi, X. Wu, S. Wang, Y. Yi, and P. Wu, Design of ultra-narrow band graphene refractive index sensor, Sensors **22,** 6483 (2022).

[36] Y. Wang, W. Cheng, J. Qin, and Z. Han, Terahertz refractive index sensor based on the guided resonance in a photonic crystal slab, Opt. Commun. **434,** 163 (2019).

[37] W. Pan, Y. Yan, Y. Ma, and D. Shen, A terahertz metamaterial based on electromagnetically induced transparency effect and its sensing performance, Opt. Commun. **431,** 115 (2019).

[38] Z. Li, Z. Yi, T. Liu, L. Liu, X. Chen, F. Zheng, J. Zhang, H. Li, P. Wu, and P. Yan, Three-band perfect absorber with high refractive index sensing based on an active tunable Dirac semimetal, Phys. Chem. Chem. Phys. **23,** 17374 (2021).

[39] A. S. Saadeldin, M. F. O. Hameed, E. M. A. Elkaramany, and S. S. A. Obayya, Highly sensitive terahertz metamaterial sensor, IEEE Sens. J. **19,** 7993 (2019).

[40] Q. Xie, G.-X. Dong, B.-X. Wang, and W.-Q. Huang, High-Q Fano resonance in terahertz frequency based on an asymmetric metamaterial resonator, Nanoscale Res. Lett. **13,** 1 (2018).

[41] H. Liang, T. Shen, Y. Feng, H. Liu, and W. Han, A D-shaped photonic crystal fiber refractive index sensor coated with graphene and zinc oxide, Sensors **21,** 71 (2021).

[42] X. Yan, R. Fu, T. Cheng, and S. Li, A highly sensitive refractive index sensor based on a V-shaped photonic crystal fiber with a high refractive index range, Sensors **21,** 3782 (2021).

[43] W. Lin, W. Huang, Y. Liu, X. Chen, H. Qu, and X. Hu, Cladding mode fitting-assisted automatic refractive index demodulation optical fiber sensor probe based on tilted fiber Bragg grating and SPR, Sensors **22,** 3032 (2022).

[44] https://rscf.ru/en/project/21-79-30038/

[45] https://rscf.ru/project/21-72-30018/

[46] E. Nenasheva, N. Kartenko, I. Gaidamaka, O. Trubitsyna, S. Redozubov, A. Dedyk, and A. Kanareykin, Low loss microwave ferroelectric ceramics for high power tunable devices, J. Eur. Ceram. Soc. **30,** 395 (2010).

[47] R. D. P.-D. i Yague, A. B. Ibars, and L. F. Martínez, Analysis and reduction of the distortions induced by time-domain filtering techniques in network analyzers, IEEE Trans. Instrum. Meas. **47,** 930 (1998).

[48] R. G. Newton, Optical theorem and beyond, Am. J. Phys. **44,** 639 (1976).

[49] C. F. Bohren and D. R. Huffman, *Absorption and Scattering of Light by Small Particles* (Wiley-VCH, Weinheim, 2008).

[50] M. F. Limonov, M. V. Rybin, A. N. Poddubny, and Y. S. Kivshar, Fano resonances in photonics, Nat. Photonics **11,** 543 (2017).

[51] A. A. Bogdanov, K. L. Koshelev, P. V. Kapitanova, M. V. Rybin, S. A. Gladyshev, Z. F. Sadrieva, K. B. Samusev, Y. S. Kivshar, and M. F. Limonov, Bound states in the continuum and Fano resonances in the strong mode coupling regime, Adv. Photonics **1,** 016001 (2019).

[52] K. Ladutenko and A. Shalev, Fano fitting tool, https://github.com/ArtyomShalev/fano_fitting_tool (2022).